RSC Advances

ROYAL SOCIETY OF CHEMISTRY

www.rsc.org/advances

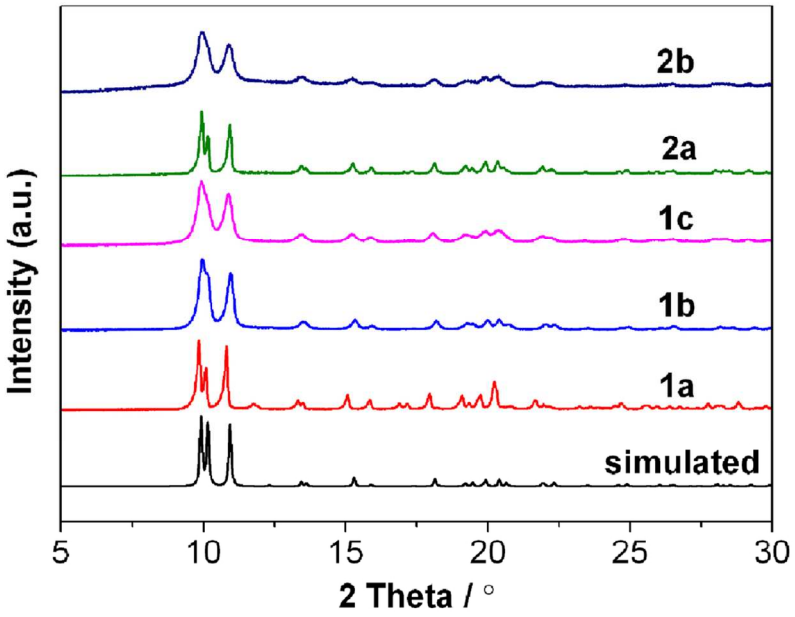

Fig. 1 Comparison of the experimental powder X-ray diffraction patterns of synthesized [Ni3(HCOO)6] samples along with the simulated pattern from Reference [55].
58x41mm (600 x 600 DPI)

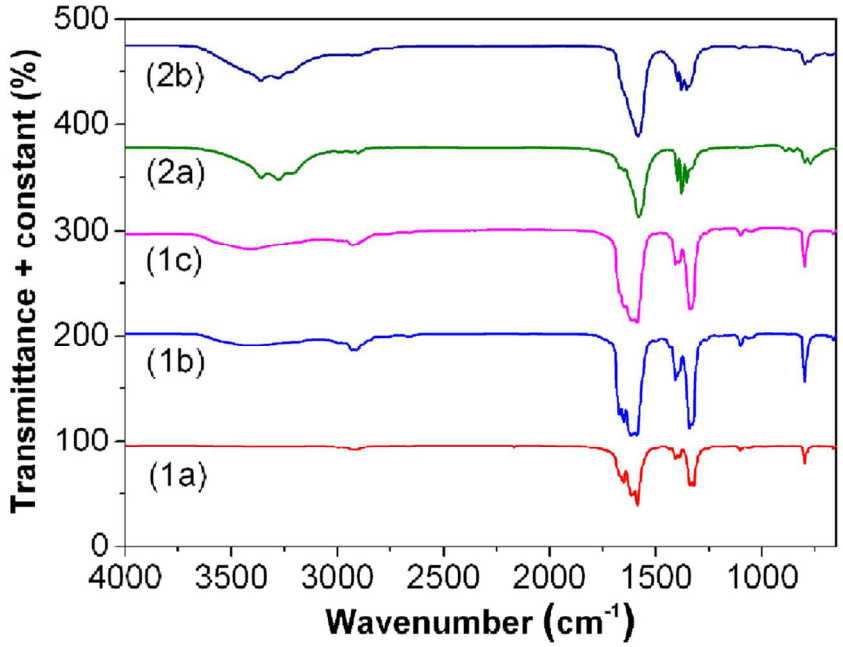

Fig. 2 FT-IR spectroscopy of [Ni3(HCOO)6] samples.
58x41mm (600 x 600 DPI)

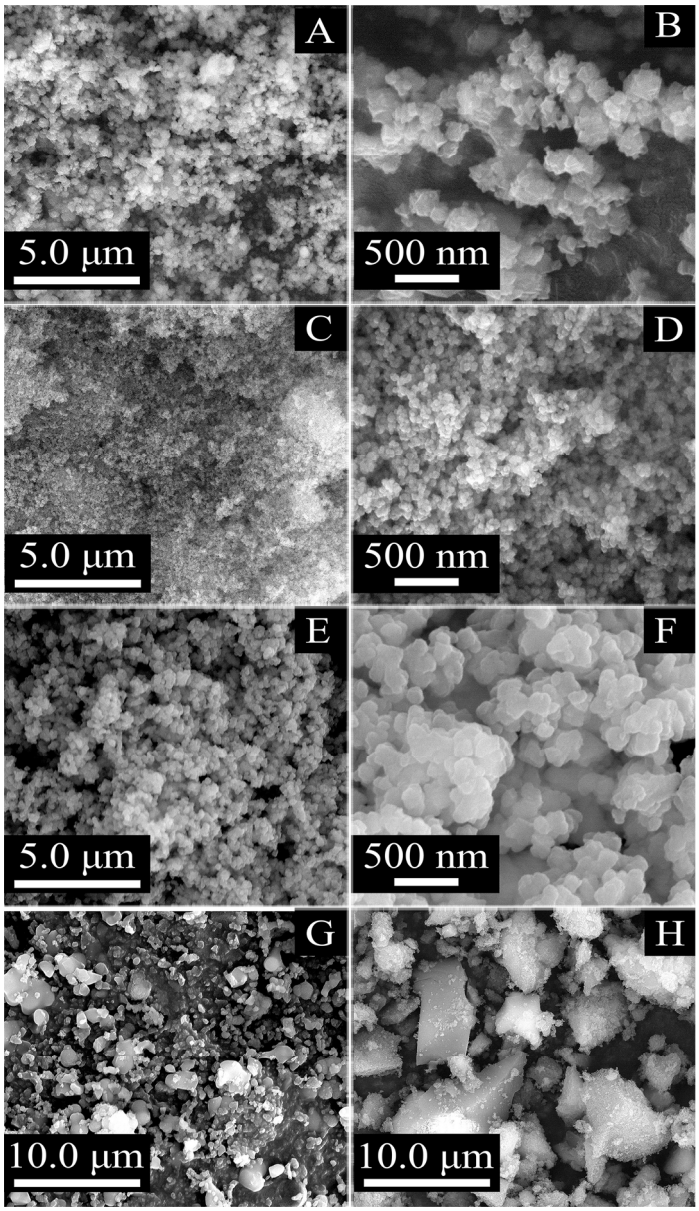

Fig. 3 SEM images of [Ni3(HCOO)6] samples: (A) and (B) 1a, (C) and (D) 1b, (E) and (F) 2a, (G) 1c and (H) 2b.
144x250mm (300 x 300 DPI)

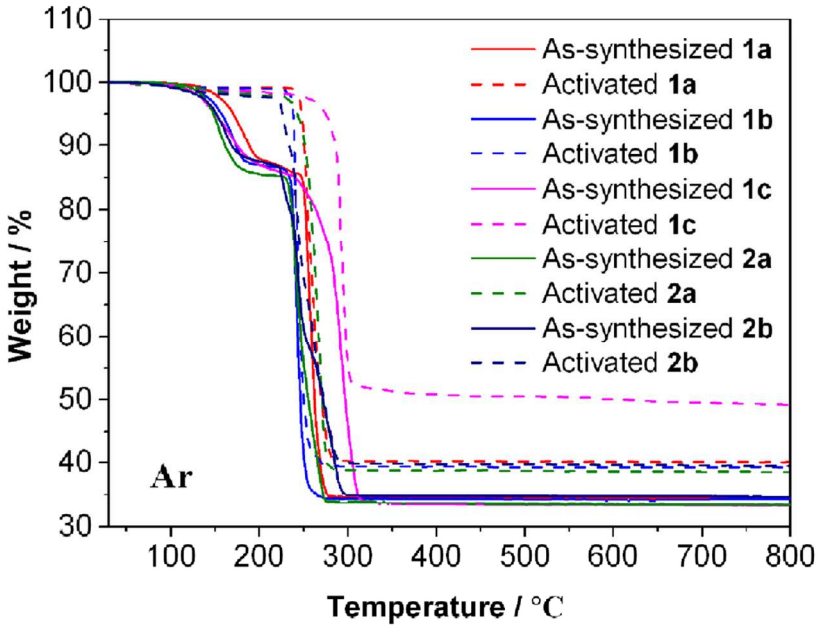

Fig. 4 TGA curves of [Ni3(HCOO)6] samples in argon atmosphere.
58x41mm (600 x 600 DPI)

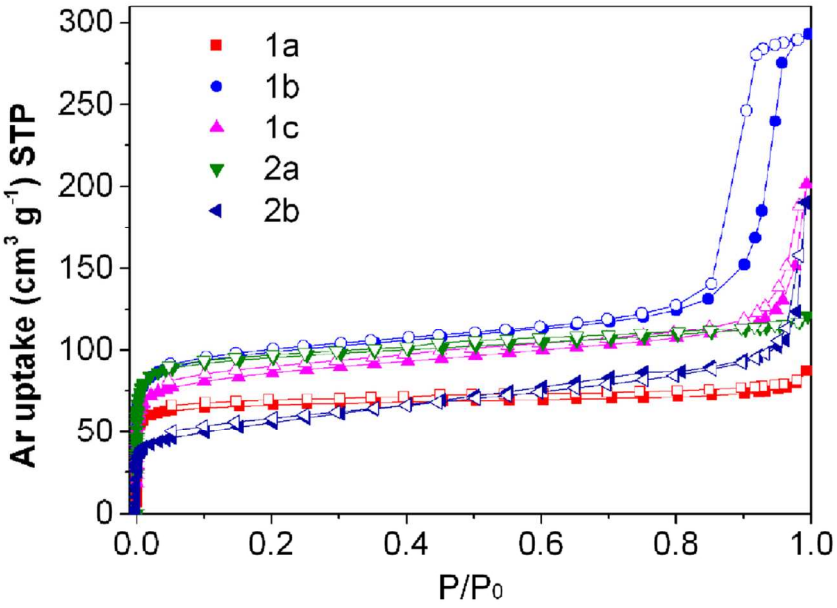

Fig. 5 Argon adsorption isotherms of [Ni3(HCOO)6] samples: 1a (red squares); 1b (blue circles); 1c (magenta up triangles); 2a (olive down triangles) and 2b (navy left triangles) measured at 87.3 K, respectively.
58x41mm (600 x 600 DPI)

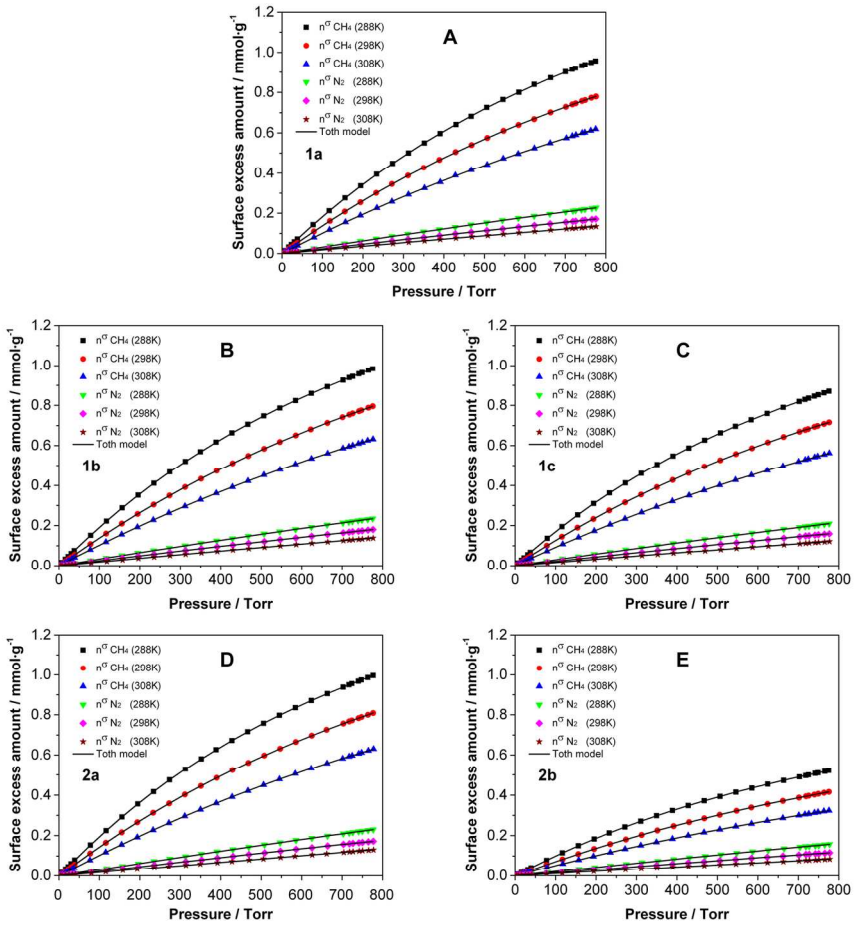

Fig. 6 Pure gas adsorption experiments: adsorption isotherms for CH4 at 288 K (black squares), 298 K (red cycles) and 308 K (blue up triangles) and N2 at 288 K (green down triangles), 298 K (magenta diamonds) and 308 K (wine stars) on (A) Sample 1a; (B) Sample 1b; (C) Sample 1c; (D) Sample 2a; (E) Sample 2b (Solid lines: Toth model). Toth model nicely fits each CH4 and N2 adsorption isotherm on [Ni3(HCOO)6] samples.
82x82mm (600 x 600 DPI)

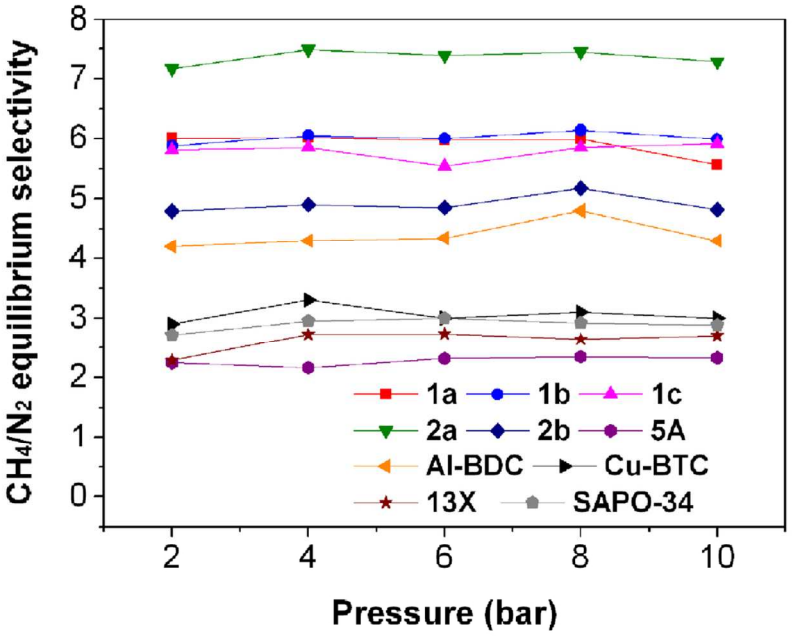

Fig. 7 CH4-N2 selectivity as a function of pressure for [Ni3(HCOO)6] samples, zeolites and other MOFs.
58x41mm (600 x 600 DPI)

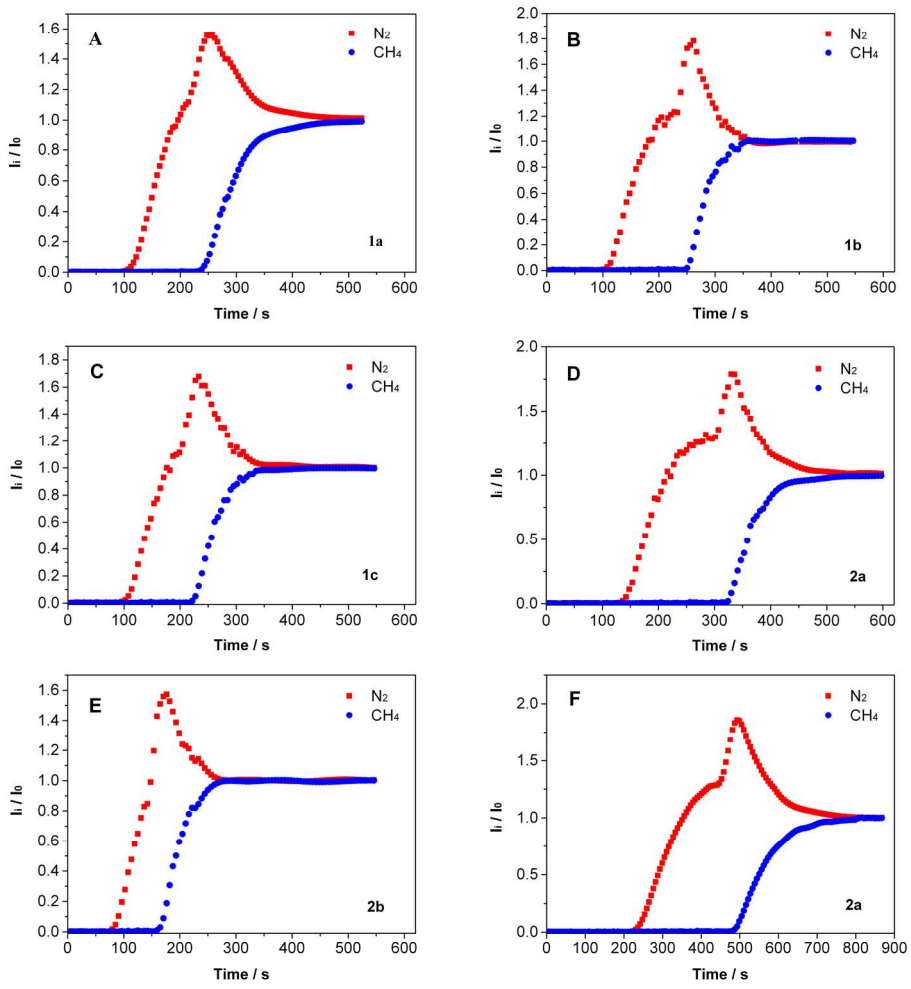

Fig. 8 Breakthrough curves of the CH4-N2 equimolar mixture on [Ni3(HCOO)6] samples at 298 K for (A) Sample 1a, (B) Sample 1b, (C) Sample 1c, (D) Sample 2a, (E) Sample 2b at 2.0 bar and (F) Sample 2a at 4.0 bar.
92x102mm (600 x 600 DPI)

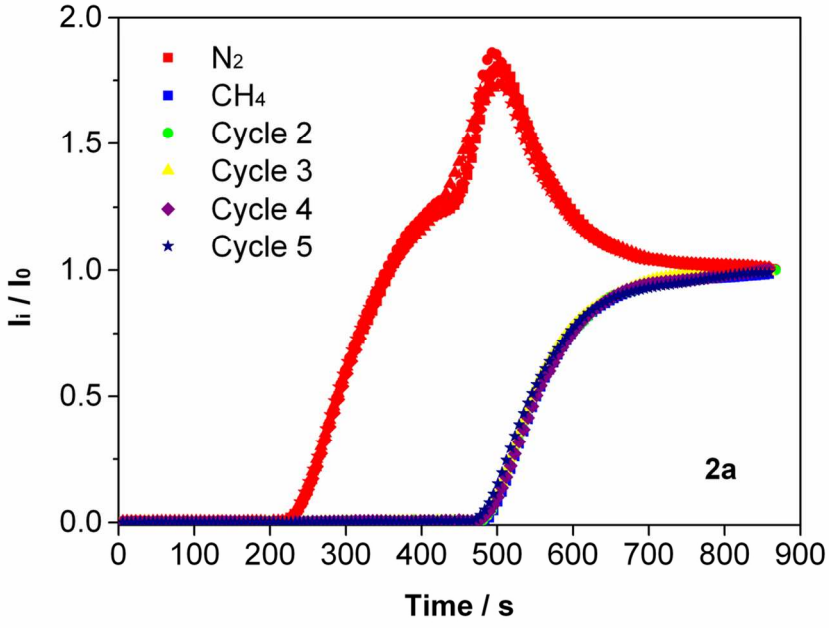

Fig. 9 Breakthrough curves on Sample 2a for five repeated cycles at 298 K and 4.0 bar.
58x41mm (600 x 600 DPI)

Textual Abstract

The adsorptive separation selectivities of CH_4/N_2 were successfully improved from 4.0−4.8 to 7.0−7.5 via synthesis optimization of the ultra-microporous $[Ni_3(HCOO)_6]$ frameworks.

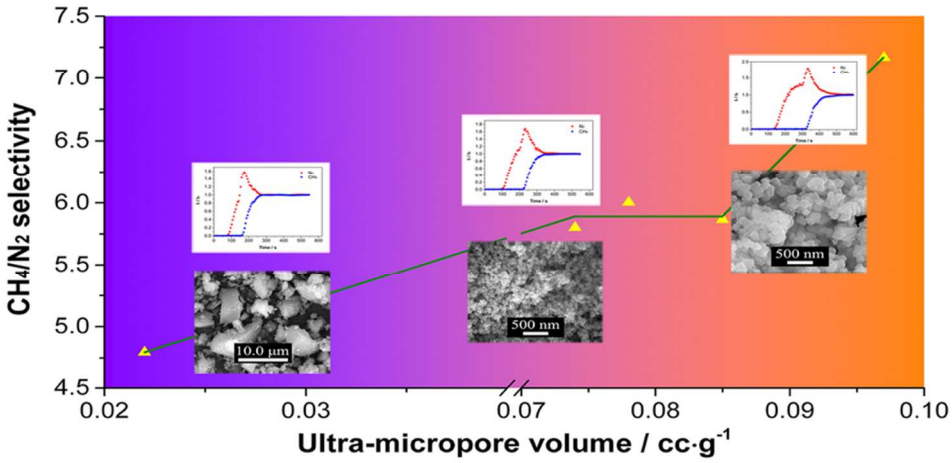

40x20mm (600 x 600 DPI)

Synthesis optimization of the ultra-microporous $[Ni_3(HCOO)_6]$ framework to improve its CH_4/N_2 separation selectivity †

Xinyu Ren,[a,b] Tianjun Sun,[*a] Jiangliang Hu,[a,b] and Shudong Wang[*a,c]

[a] Dalian National Laboratory for Clean Energy, Dalian Institute of Chemical Physics, Chinese Academy of Sciences, Dalian 116023, P. R. China.
[b] University of Chinese Academy of Sciences, Beijing 100049, P. R. China
[c] State Key Laboratory of Catalysis, Dalian Institute of Chemical Physics, Chinese Academy of Sciences, Dalian 116023, China

Corresponding Authors

[*] Telephone: +86-411-84379052; Fax: +86-411-84662365. E-mail: wangsd@dicp.ac.cn (Prof. Shudong Wang); suntianjun@dicp.ac.cn (Dr. Tianjun Sun).

† Electronic supplementary information (ESI) available. See DOI: 10.1039/b000000x/

Abstract

Separation of methane and nitrogen is an important issue in upgrading low-quality natural gas and non-cryogenic, adsorption-based separation of CH_4/N_2 is particularly challenging. In this report, a MOF adsorbent namely $[Ni_3(HCOO)_6]$ framework is comprehensively investigated for the separation of CH_4/N_2 mixture via pure gas adsorption and binary gas breakthrough experiments. All the prepared samples synthesized from different routes were also studied in detail by PXRD, FT-IR, SEM, TGA/DSC and argon adsorption. The results show that the adsorptive separation performances can be improved significantly by optimizing the synthesis of the framework. The precursors play crucial roles in the crystallization of $[Ni_3(HCOO)_6]$ frameworks, giving rise to the variability in ultra-micropore volume, surface area and pore size. Good crystallization can result in large ultra-micropore volume and furthermore brings about high separation selectivity. The $[Ni_3(HCOO)_6]$ framework synthesized by nickel nitrate and methyl formate exhibits the best crystallization and the largest micropore volume, leading to the highest CH_4/N_2 separation selectivity up to 7.5 in the pressure range of 2.0-10 bar, which is the highest value reported for MOFs. Moreover, this adsorbent presents uniform nanosized crystal (~ 140 nm), permanent porosity and consistent separation performances, making the $[Ni_3(HCOO)_6]$ framework a promising candidate for natural gas upgrading.

Keywords

Adsorption, CH_4/N_2 separation, ultra-micropore, metal-organic frameworks, natural gas upgrading

1. Introduction

Upgrading technologies of natural gas are becoming increasingly significant due to the large demand for this clean-burning and economical alternative fuel. However, gases extracted from the reservoirs contain contaminants such as heavier gaseous hydrocarbons (C2+), carbon dioxide,

hydrogen sulfide, nitrogen, water and mercury, which greatly lower the quality and need to be removed in order to meet the pipeline quality.[1,2] Among the purification processes, the nitrogen removal is technically difficult due to the similar physical and chemical properties of the methane and nitrogen molecules.[3,4] Efficiently reducing the nitrogen content of low-quality natural gas streams is one of the world's toughest energy challenges.[5-7] In general, adsorptive separation via pressure swing adsorption (PSA) process is an energy-effective and economic-feasible alternative to cryogenic distillation. Many porous materials including activated carbon,[8-11] silicalite[12,13] and molecular sieves[3,14-20] have been evaluated for CH_4/N_2 separation. However, adsorptive separation of CH_4/N_2 has been found particularly challenging because of the unsatisfactory performances for the existing adsorbents. Furthermore, compared with the numerous extensive studies on the natural gas upgrading processes like CO_2/CH_4 separations,[21-25] there is less work carried out for this particular difficult separation of CH_4/N_2 mixtures.[4,26]

Recently, metal-organic frameworks (MOFs) have been attracted remarkable attentions for their promising applications in gas storage,[25,27-30] gas purification and separation,[31-33] due to their ultrahigh specific surface area, adjustable pore sizes and controllable properties, as well as acceptable thermal stability.[34-37] A few MOFs have been evaluated on the separation of CH_4/N_2 mixtures by prediction from the pure gas adsorption isotherms or molecular simulations.[38-44] Basolite® A100 and $^3_\infty$[Cu(Me-4py-trz-ia)] were evaluated and found to exhibit selectivities of S_{CH_4/N_2} = 3.4−4.4 and S_{CH_4/N_2} = 4.0−4.4 at 298 K, respectively.[43] MOF-5 and MOF-177 were predicted to have selectivities of S_{CH_4/N_2} = 1.1 and S_{CH_4/N_2} = 4.0 at 298 K, respectively.[39] The simulated selectivities for HKUST-1, IRMOF-1, IRMOF-11, IRMOF-12, UMCM-1, UMCM-2, ZIF-68 and ZIF-69 are 2.0−4.0 at pressures up to 2.0 MPa and 298 K.[40-42] However, the adsorption selectivities of CH_4 over N_2 on these MOFs are not superior to those of the conventional adsorbents like activated carbon and zeolites.[8-20]

In the earlier work, we studied the selective adsorption of CH_4 against N_2 on two ultra-microporous frameworks, $[M_3(HCOO)_6]$ (M = Ni, Co), and confirmed that both the

frameworks have high selectivities for the separation of CH_4/N_2 mixtures, especially the $[Ni_3(HCOO)_6]$ with highly enhanced selectivities up to 6.5.[44] The high selectivity is engendered by the tight coupling between uniform ultra-micropore (< 7 Å) and moderate polarizability.[1,43,45-47] The ultra-micropore walls are in proximity to each other, providing an enhanced adsorption potential towards gas molecules of the similar size within the micropores.[46,47] It is known that differences in synthesis procedures will have great effects on the pore structure and morphology of metal-organic frameworks, which are key features to evaluate gas adsorption characteristics.[48,49] As a continuation of our previous study for the separation of CH_4/N_2 on the $[Ni_3(HCOO)_6]$ framework and a step toward the development of novel CH_4−selective adsorbents, here we report the synthesis of $[Ni_3(HCOO)_6]$ frameworks from different routes to tune the ultra-micropore volume and improve the performances of the selective adsorption of CH_4 against N_2. The separation selectivity of the optimized $[Ni_3(HCOO)_6]$ framework with high ultra-micropore volume and good crystallinity can be improved to 7.5 at 298 K and 4.0 bar, which is the highest value ever reported for CH_4/N_2 separation on MOFs. Moreover, the modified synthesis is easy to scale up because the usage of methyl formate instead of formic acid will not only overcome the corrosion problem of formic acid, but also shorten its synthetic route in industry as formic acid is derived from the hydrolysis of methyl formate in industrial practice. We believe that such study is vital to understand the effect of synthesis procedure on pore structure and adsorption characteristics of $[Ni_3(HCOO)_6]$ frameworks, as well as natural gas upgrading. The fundamental studies will be helpful for the optimization of this new adsorbent with high ultra-micropore volume and excellent separation performance for practical CH_4/N_2 separation.

2. Experimental

2.1 Material synthesis. All solvents and reagents in this work were of analytical grade quality obtained from commercial sources and used without further purification unless otherwise stated. Formic acid [FA, HCOOH, 98.0%], methyl formate [MF, $HCOOCH_3$, 98.0%], nickel nitrate hexahydrate [$Ni(NO_3)_2{\cdot}6H_2O$, 98.5%], nickel acetate tetrahydrate [$Ni(CH_3COO)_2{\cdot}4H_2O$, 98.0%]

and nickel chloride hexahydrate [$NiCl_2 \cdot 6H_2O$, 98.0%] were purchased from Sinopharm Chemical Reagent Co., Ltd., Shanghai, China. *N*,*N*-dimethylformamide [DMF, 99.5%] and acetone [$CO(CH_3)_2$, 99.5%] were purchased from Tianjin Kermel Chemical Reagent Co., Ltd., Tianjin, China.

2.1.1 Hydrothermal synthesis from formic acid (FA). Sample **1a**, **1b** and **1c** series were synthesized using modified solvothermal conditions by very similar methods.[50] The preparation of Sample **1a** is described as an example. A homogenous mixture of nickel nitrate hexahydrate (5.678 g, 19.5 mmol) and formic acid (5 ml, 129.9 mmol) in DMF (40 ml) was transferred into a 150 ml Teflon-lined stainless steel autoclave and heated (under autogenous pressure) in an oven at 373 K for 48 h. After cooling naturally, the light green crystalline powdery product was separated by centrifugation at 10000 rpm for 5 min and rinsed with DMF (10 ml) and acetone (10 ml). Then the resultant product was dried in a vacuum oven at 323 K for 2 h. Yield: 3.29 g, 100% based on nickel nitrate.

Sample **1b** and **1c** were obtained by similar procedures except for the different nickel salts, where nickel acetate tetrahydrate (4.852 g, 19.5 mmol) for Sample **1b** and nickel chloride hexahydrate (4.635 g, 19.5 mmol) for Sample **1c** were used in yields of 97.8% and 95.1%, respectively.

2.1.2 Hydrothermal synthesis from methyl formate (MF). Sample **2a**, **2b** and **2c** series were synthesized via very similar methods. The preparation of Sample **2a** is described as an example. A 40 ml DMF solution containing 5.678 g nickel nitrate hexahydrate (19.5 mmol) and 8.2 ml methyl formate (130.0 mmol) was transferred into a 150 ml Teflon-lined stainless steel autoclave and heated (under autogenous pressure) in an oven at 373 K for 48 h. After cooling naturally, the light green crystalline powdery product was separated by centrifugation at 10000 rpm for 5 min and rinsed with DMF (10 ml) and acetone (10 ml). Then the resultant product was dried in a vacuum oven at 323 K for 2 h. Yield: 3.29 g, 100% based on nickel nitrate.

Sample **2b** and **2c** were obtained by similar procedures except for the different nickel salts,

where nickel acetate tetrahydrate (4.852 g, 19.5 mmol) for Sample **2b** and nickel chloride hexahydrate (4.635 g, 19.5 mmol) for Sample **2c** were used in yields of 100% and 1.69%, respectively. The yield of Sample **2c** is too low to get enough quantities to study further.

The as-synthesized samples of $[Ni_3(HCOO)_6 \cdot DMF]$ were evacuated in a vacuum oven at 433 K (higher than the boiling point of DMF, 426 K) for 12 h. The resulting void-cleaned samples of $[Ni_3(HCOO)_6 \cdot DMF]$ were referred to as the "activated samples", namely $[Ni_3(HCOO)_6]$ as well as Ni formate.

2.2 Characterization. Powder X-ray diffraction (XRD) patterns of all samples were obtained on a PANalytical X'pert diffractometer (Cu Kα, 40 kV, 40 mA) for 2θ values from 5° to 30° with a step size of 0.01° and a scan rate of 5° min^{-1}. Fourier transform infrared (FTIR) spectra data were recorded in the frequency range of 4000−650 cm^{-1} with a resolution of 4 cm^{-1} on a Nicolet 6700 spectrometer in transmittance mode at room temperature. All the samples were ground with KBr, and pressed into thin discs. The crystal morphologies of the synthesized product were examined using a scanning electron microscope (SEM, Quanta 200F, FEI Company). Thermal gravimetric analysis (TGA) and differential scanning calorimetry (DSC) were performed to study the thermal stability of the products using a NETZSCH STA 449 F3 analyzer under argon atmosphere (20 ml min^{-1}, 30−800 °C, 10 °C min^{-1}) and air (20 ml min^{-1}, 30−800 °C, 10 °C min^{-1}). Pore structure analysis of the samples were conducted by low-pressure gas adsorption experiments ($1 \times 10^{-7} \leq P/P_0 \leq 1.0$) with argon (87.3 K), carried out on a Quantachrome Autosorb-iQ2 automatic volumetric instrument. The experimental apparent specific surface area, S_{BET} (Brunauer-Emmett-Teller method), the micropore volume, V_{mic} (*t*-plot method), the total pore volume, V_t (Gurvich-rule) and pore size distributions (PSD) were calculated from the Ar adsorption isotherms. Prior to the gas adsorption measurements, all the samples were outgassed at 433 K for 12 hours under turbomolecular pump vacuum.

2.3 Adsorption measurements. Pure gas adsorption and binary breakthrough experiments were carried out to evaluate the static and dynamic CH_4 adsorption capacity and selectivity against N_2.

2.3.1 Pure gas adsorption measurements. The single component adsorption isotherms of methane and nitrogen on $[Ni_3(HCOO)_6]$ frameworks were measured volumetrically (up to 760 torr) at three temperatures (288 K, 298 K and 308 K) by Autosorb-iQ2 equipped with a recirculating water bath. Sample outgassing process was carried out at 413 K under a vacuum for 12 h. The free space of the system was determined by using the helium gas. High purity grade CH_4 (99.99%), N_2 (99.999%) and He (99.999%) were used. All the methane and nitrogen adsorption isotherms have been calculated based on the three parameter Toth equation[51]

$$\theta = \frac{N}{N_{\max}} = \frac{B \times P}{(1 + (B \times P)^c)^{1/c}} \quad (1)$$

Where N is the gas uptake (mmol g^{-1}), $N_{\max}$ is the maximum gas uptake (mmol g^{-1}), B and c are fitting constants; the Henry's law constant K_H of the Toth isotherm equation can be calculated by the equation

$$K_H = \frac{dN}{dP}_{P \to 0} = N_{\max} \times B \quad (2)$$

The ideal selectivity $S_{i,j}$, also known as Henry's law selectivity, is calculated as the ratio of Henry's law constants from pure gas adsorption isotherms of gas component i and j

$$S_{i,j} = \frac{K_{H,i}}{K_{H,j}} \quad (3)$$

2.3.2 Binary gas breakthrough separation experiments. Breakthrough separation experiments were performed in a chromatographic column packed with *ca.* 3.5 ml of $[Ni_3(HCOO)_6]$ sample particles, using a homemade apparatus (see ESI, Fig. S1†). The column (a stainless steel column of 250 mm with an inner diameter of 4 mm) was placed in the oven to control the temperature. The pre-activated $[Ni_3(HCOO)_6]$ powder was pressed by a pressure of *ca*. 100 bar. Then the pellets were broken and sieved to obtain particles with diameters from 180 to 280 μm. The column was filled with the obtained particles and used as the fixed adsorption bed to record the CH_4/N_2 mixture breakthrough curves. Before each breakthrough experiment, the sample in the column was activated and outgassed in situ at 433 K for 2 h under a helium flow of 20.0 sccm. The

CH_4/N_2 breakthrough experiments were conducted at 298 K with increasing pressure up to 1.0 MPa and constant gas mixture composition (50-50 CH_4-N_2). The effluent was analyzed using a TOF-MS 500 mass spectrometer made by *Dalian Institute of Chemical Physics*. The signal strength of mass spectrometer has a good linear relationship with the molar concentration of gas in the range 0-10%. For all experiments, a permanent dilution helium flow of 40 times of the quantity of feed gas was introduced to control the molar concentration of the gas into the mass spectrometer. The sample column was purged with helium after finishing the adsorption step in every measurement to regenerate for another measurement. The pressure drop over the column was always less than 0.005 MPa. The breakthrough experiments allowed us to calculate the equilibrium selectivity or separation factor for CH_4/N_2 separation, which is defined as

$$\alpha_{i,j} = \frac{q_i / y_i}{q_j / y_j} \tag{4}$$

Where q_i is the adsorbed amount of component i and y_i is the mole fraction of component i in the gas phase. The adsorbed amount q_i was determined by integration of the experimental breakthrough curves,[52] as follows:

$$q_i = \frac{F\left(C_{i,0}t_f - \int_0^{t_f} C(t)dt\right) - V_d}{m_{ads.}} \tag{5}$$

Where F is the total flow of the feed gas passing through the column, $C(t)$ is the concentration of component i in the gas phase, t_f is the first moment of the breakthrough curve of component i leaving the column, V_d is the dead volume of the set-up. It is important to take into account the dead volume to determine the accurate adsorbed amount of components. For validation of the set-up, additional breakthrough measurements with CH_4/N_2 mixtures up to 1.0 MPa at 298 K on two commercially available MOFs of Al-BDC (Basolite® A100) and Cu-BTC (Basolite® C300) were carried out. Very good agreement between literature data and the results of this study was obtained.

3. Results and discussion

3.1 Synthesis of $[Ni_3(HCOO)_6]$ frameworks and structural characterization. In the synthesis of

MOFs, different precursors could result in different samples with various yields and diverse structure characteristics including morphology, crystal size and pore width, or even different MOFs.[48] As seen from Table 1, all synthesized samples are in high yields with the exception of Sample **2c** from nickel chloride and methyl formate.

X-ray powder diffraction analysis was first carried out to investigate the purity and crystallite structure of $[Ni_3(HCOO)_6]$ frameworks synthesized from different routes. As shown in Fig. 1, the XRD profiles of the synthesized $[Ni_3(HCOO)_6]$ samples and the simulated form show similar patterns, which are the same of samples as reported before.[50,53,54] For Sample **1a** and **2a**, the XRD patterns match perfectly with the simulated pattern, indicating that the $[Ni_3(HCOO)_6]$ frameworks synthesized from the nickel nitrate keep the better crystalline structure compared with samples synthesized from other nickel salts. On the contrary, Sample **1c** and **2b** present different XRD patterns and exhibit poor crystalline structures. For Sample **1b**, however, the pattern is transitional between the good crystalline structures and the poor ones. This can be seen from the percent crystallinity data calculated from the XRD patterns as well. As listed in Table 1, the percent crystallinities of Sample **1a** and **2a** are more than 99%, while the value for Sample **2b** is only 82.57%. For Sample **1b**, the percent crystallinity is 94.06%, between the values of Sample **2a** and **2b**.

Fourier transform infrared (FT-IR) spectroscopy of $[Ni_3(HCOO)_6]$ samples are given in Fig. 2, exhibiting the similar frameworks for the synthesized samples. The split weak bands around 2900 cm^{-1} are caused by the stretching vibrations of C−H in the six individual $HCOO^-$ groups in the structure. The strong bands at 1355−1325 cm^{-1} and 1650−1580 cm^{-1} can be ascribed to the ν_{as}(C−O) and ν_s(C−O) vibrations of the $-COO^-$ groups.[49] A pair of medium intense bands at 1408−1399 cm^{-1} and 1393−1378 cm^{-1} are attributed to asymmetric deformation vibrations of O−C−O.[55] The medium intense peak around 800 cm^{-1} can be assigned to the symmetric deformation vibrations of O−C−O.[55]

For the IR spectra of Sample **1a**, **1b** and **1c** synthesized from formic acid, besides the bands from the bridging formate ligands, the additional bands around 1100 cm^{-1} and 1680 cm^{-1} are due to

the *v*(C−N) and *v*(C=O) vibrations of DMF molecules, which indicate that DMF molecules are still left in the channels because of incomplete activation.[49] While for Sample **2a** and **2b** synthesized from methyl formate, there is no band attributed to the DMF molecules, demonstrating the two samples are well activated. Their IR spectra exhibit broad bands in the region between 3400−3100 cm^{-1}, which are due to *v*(O−H) vibrations of the uncoordinated water molecules involved in weak hydrogen bonds, indicating that moisture in the atmosphere is re-adsorbed in the activated samples of **2a** and **2b**.[54] This phenomenon indicates that the $[Ni_3(HCOO)_6]$ samples synthesized from methyl formate are easier to remove the guest molecules (DMF) to get the activated forms.

3.2 Morphologies of $[Ni_3(HCOO)_6]$ frameworks. The SEM images of the synthesized $[Ni_3(HCOO)_6]$ samples are shown in Fig. 3. Apparently seen from the images, Sample **1a**, **1b** and **2a** exhibit uniform crystals while Sample **1c** and **2b** show heterogeneous morphologies. More specifically, uniform crystals with the size of ~ 140 nm are observed from Fig. 3E and 3F for Sample **2a**, which agrees well with the highest crystallinity data as calculated from the XRD pattern (Table 1). Smaller crystal size of ~ 75 nm can be obtained for Sample **1b** (Fig. 3C and 3D), which is almost half the size of Sample **2a**. The smaller crystallite size produces broader peaks in the XRD patterns for Sample **1b**.[56] However, based on the non-uniform crystals of Sample **1c** showed in Fig. 3G and the low yield of **2c**, we can conclude that using nickel chloride as the nickel precursors is unfavorable for the synthesis of uniform $[Ni_3(HCOO)_6]$ crystals. Nevertheless, the heterogeneity of Sample **2b** crystals with the size of as large as 12.5 μm shown in Fig. 3H indicates that the combination of nickel acetate and MF as precursors seems like a poor choice, resulting in worse crystallinity (82.57%). Accordingly, the precursors have great influences on the crystal growth. This also suggests us a feasible strategy to manipulate the size and morphology of MOF crystals by changing the metal and organic linker precursors.

3.3 Chemical and thermal stability analysis. High thermal stability and inertness to different solvents are some of essential requirements for the application of MOFs used as adsorbents. Therefore, the thermal behaviors of the as-synthesized and activated $[Ni_3(HCOO)_6]$ samples were

investigated by using thermal analysis (TGA/DSC) (Fig. 4 and see ESI, Fig. S2−S13†). Both in argon and air atmosphere, there are two clear weight loss steps for all the as-synthesized $[Ni_3(HCOO)_6]$ samples with one step for guest removal and the other for framework collapse, while there is only one rapid weight loss step for all the absolute activated samples in the absence of guest removal step. All the samples reveal a thermal stability range up to *ca*. 230 °C in argon atmosphere and *ca*. 250 °C in air atmosphere. Specifically, the TGA trace for as-synthesized Sample **2a** in argon atmosphere shows a gradual weight-loss step between 120 °C and 200 °C, which corresponds to the removal of the DMF guest molecules (calculated: 14.07%; observed: 14.05%), along with an endothermic enthalpy of 113.5 kJ/mol, calculated according to the DSC curves (Fig. S6). A plateau between 200 °C and 230 °C indicates that the evacuated framework has high thermal stability (Fig. 4). The second rapid weight loss of *ca.* 51.42%, starting at 230 °C and ending at 280 °C, implies the collapse of the framework with an endothermic enthalpy of 166.2 kJ/mol. Compared with the as-synthesized **2a**, the activated **2a** shows only one clear weight loss process at a similar temperature (230−280 °C, 58.85%, 188.2 kJ/mol). The similar weight loss processes are observed for **2a** in air atmosphere. Two weight loss steps (100−230 °C, 15.17%; 230−300 °C, 43.06%) are observed for the as-synthesized Sample **2a**, and only one rapid weight loss (240-300 °C, 48.36%) occurs for the guest-free sample. Additionally, this weight loss process becomes exothermic (Fig. S11†), and the exothermic enthalpy for framework decomposition in air is 616.4 kJ/mol. The samples of **1a**, **1b**, **1c** and **2b** share the similar thermal behavior with Sample **2a**. All the guests (adsorbed water molecule in the air and DMF) are liberated from the pores up to *ca*. 250 °C both in argon and air atmosphere, then the frameworks decompose up to *ca*. 300 °C.

Chemical stability of the $[Ni_3(HCOO)_6]$ framework was evaluated by the heating the sample in DMF, methanol, ethanol and water at 100 °C for 24 hours. These conditions generally reflect potential extreme industrial requirements. Take the Sample **2a** as an example, the sample retained its framework structure under these conditions, as evidenced by the sharp, unshifted diffraction lines in the PXRD patterns in Fig. S13 (see ESI†). For samples treated by ethanol and water,

however, the crystallinities were reduced a little. Further investigation was carried out to evaluate the pore structure change for the sample treated by water via Ar (87 K) adsorption experiment. As showed in Fig. S14 (see ESI†), there was little change in micropore structure for the $[Ni_3(HCOO)_6]$ framework indicating a good chemical stability in water.

3.4 Pore structure analysis. Argon adsorption measurements were carried out under liquid argon bath (87.3 K) to evaluate the porosity of $[Ni_3(HCOO)_6]$ samples (Fig. 5). The BET surface area is calculated from the Ar adsorption isotherms with good linearity.[57] The total pore volume and micropore volume are calculated using Gurvich-rule and *t*-Plot method, respectively.[58] The texture properties are summarized in Table 2. All the Ar adsorption isotherms of $[Ni_3(HCOO)_6]$ samples exhibit initial type-I isotherm and the increase in the volume adsorbed at very low relative pressures corresponding to a permanent microporosity. However, for Sample **1b**, the isotherm shifts to type-IV with a significant portion of the mesopore volume, which may be attributed to the interparticle voids of the nanoparticle agglomeration.[58] The BET surface area and total pore volume is 331 $m^2\ g^{-1}$ and 0.350 $cm^3\ g^{-1}$, higher than other samples. The mesopores in Sample **1b** make contributions to the higher BET surface area and larger total pore volume. However, the micropore volume which is essential to the separation of small gas molecules is 0.085 $cm^3\ g^{-1}$, equivalent to the values for Sample **1a** and **1c**.[43,46] For comparison, the BET surface area and the micropore volume for Sample **2b** are only 173 $m^2\ g^{-1}$ and 0.022 $cm^3\ g^{-1}$, much lower than other samples. This could be attributed to crystal imperfections as indicated by the PXRD patterns (Fig. 1 and Table 1). The increase in the volume adsorbed near $P/P_0 = 1$ for Sample **2b** is ascribed to the existence of the macropores resulting from the stacking of the large crystals,[59] which can be seen form the SEM images (Fig. 3). For Sample **2a**, the BET surface area, the total pore volume and the micropore volume is 327 $m^2\ g^{-1}$, 0.146 $cm^3\ g^{-1}$ and 0.097 $cm^3\ g^{-1}$, respectively. Obviously, the micropore volume of Sample **2a** is higher than other samples, which makes Sample **2a** more suitable for the separation of CH_4 and N_2.[43,44] In order to estimate pore size distributions for $[Ni_3(HCOO)_6]$ samples, Ar isotherms were analyzed using non-local density functional theory (NLDFT) applying a hybrid

kernel for Ar adsorption at 87 K. The analysis of $[Ni_3(HCOO)_6]$ samples result in good fittings with the least fitting errors. The zigzag micropore sizes of the $[Ni_3(HCOO)_6]$ frameworks are estimated *ca.* 6 Å from Ar adsorption isotherms, with an additional mesopore distribution at *ca.* 21.3 nm for Sample **1b**. Nevertheless, Sample **2b** presents a shift of micropore size with two peaks centered at 8.30 Å and 1.87 nm. The micropore size is beyond ultra-micropore size range (< 7 Å) which may be unfavorable for the separation of small gas molecules.[44] The results suggest that the pore structure of $[Ni_3(HCOO)_6]$ frameworks including the ultra-micropore volume, pore size and surface area can be adjusted by changing the precursors, which may be giving rise to different gas adsorption behaviors and separation performances.

3.5 Pure gas adsorption isotherms. The adsorption isotherms of CH_4 and N_2 were measured at 288 K, 298 K and 308 K on $[Ni_3(HCOO)_6]$ samples to evaluate the separation capability for CH_4/N_2 mixtures (Fig. 6). The ultra-micropore volumes of the frameworks are acting as gas adsorption sites.[47] As list in Table 2, the CH_4 and N_2 adsorption amounts for $[Ni_3(HCOO)_6]$ samples are consistent with the micropore volume. Sample **2a** which has the largest micropore volume (0.097 $cm^3\ g^{-1}$) adsorbs the largest amount of CH_4 (0.81 mmol g^{-1} at 1.0 bar and 298 K) while Sample **2b** adsorbs the least amount of CH_4 (0.42 mmol g^{-1}) due to its least micropore volume (0.022 $cm^3\ g^{-1}$). A comparison of the adsorbed amounts of CH_4 and N_2 for Sample **1a**, **1b** and **1c** reveals that equivalent micropore volume leads to the equivalent adsorption amount. Additionally, for Sample **1b**, the large percentage of mesopore volume also makes contributions for the adsorbed amounts of both CH_4 and N_2 to some extent. However, the mesopores with the size of 21.3 nm are too large and non-selective for the separation of CH_4 and N_2 molecules. On the whole, the large adsorption amount of the CH_4 and N_2 are dominantly determined by the ultra-micropore volume since the ultra-micropore have an enhanced adsorption potential towards gas molecules within the micropores.[60]

Clearly seen from Fig. 6, CH_4 is preferentially adsorbed over N_2 for all the $[Ni_3(HCOO)_6]$ samples due to the higher uptakes of CH_4 against N_2. This is probably attributed to the fact that CH_4

molecules have a higher polarizability (26×10^{-25} cm^{-3} for CH_4 *vs.* 17.6×10^{-25} cm^{-3} for N_2) and are more polarisable than N_2 molecules. Although N_2 molecules exhibit a quadrupole moment, it is of less influence regarding the total adsorption potential than their difference in polarizability.

All the adsorption data are fitted well with Toth model. The parameters of the fitting procedures are given in Table S1−S5 (see ESI†). According to the Henry's law constants calculated from the pure gas adsorption isotherms, all the $[Ni_3(HCOO)_6]$ samples favor CH_4 more than N_2 since higher values of Henry's law constants for CH_4 adsorption correspond to higher adsorption potential towards CH_4 for all samples. The preferential adsorption of CH_4 over N_2 leads to an equilibrium adsorption selectivity of CH_4 higher than $\alpha_{CH_4/N_2} = 1$.[43] Accordingly, the ideal adsorption selectivities of separating CH_4/N_2 mixtures are calculated as the ratio of the Henry's law constants from the pure gas isotherms on the $[Ni_3(HCOO)_6]$ samples. All the calculated ideal selectivities at 288 K, 298 K and 308 K are given in Table 3. The ideal selectivities for all the samples are nearly constant between 288 K and 308 K. Thus, the temperature dependence of the experimentally determined selectivities is very small in the investigated temperature range and can be neglected.[43] Sample **1a**, **1b** and **1c** exhibit the similar ideal selectivities S_{CH_4/N_2} between 5.7 and 6.1, which is the consequence of the equivalent micropore volume. For Sample **2a**, the selectivities are between 6.2 and 6.6, which are among the highest values reported for MOFs in CH_4/N_2 separation. The large ultra-micropore volume accounts for the high selectivities. Lower selectivities between 4.7 and 4.8 are calculated for Sample **2b** because of the low micropore volume. In the meanwhile, the micropore size of Sample **2b** shifts to 8.30 Å and 1.87 nm, beyond the ultra-micropore size range of gas molecule dimensions (< 7 Å), which is not preferential for the separation of small gas molecules (CH_4: 3.80 Å, N_2: 3.64 Å).[47] It is safe to conclude that larger ultra-micropore volume corresponds to the higher selectivities. The high selectivities predicted from the pure gas adsorption isotherms indicate that Sample **2a** has the great potential in separation of CH_4/N_2 and is a promising candidate for nitrogen removal from natural gas. Moreover, it is noted that the Sample **2a** is sufficiently stable and robust, as we could perform a whole series of sorption

measurements without changing the sample, even after long exposures to humid air.

3.6 Binary gas breakthrough separation experiments. To confirm the selective adsorption of CH_4 over N_2 on $[Ni_3(HCOO)_6]$ samples, binary gas breakthrough separation experiments were conducted under different pressures from 2.0 to 10 bar at 298 K. Additionally, two commercially available MOFs of Al-BDC (Basolite® A100) and Cu-BTC (Basolite® C300) were examined on the separation of CH_4/N_2 mixtures for comparison, validating the breakthrough set-up as well (see ESI, Fig. S15 and S16†). Zeolites including 5A, 13X and SAPO-34 were also investigated (Fig. S17–S19†). A binary mixture composing 50% of CH_4 and 50% of N_2 were used as feed gas to investigate the separation performance of the adsorbents.

Fig. 7 shows the selectivities for CH_4 over N_2 determined from the breakthrough experiments on different adsorbents. At the range of 2.0−10 bar, Cu-BTC MOF exhibits selectivity of α_{CH_4/N_2} = 2.9−3.1, which agrees well with the simulated selectivity around α_{CH_4/N_2} = 3.0−3.5 in literature,[40] and Al-BDC MOF shows selectivity of α_{CH_4/N_2} = 4.2−4.8, which coincides with the value α_{CH_4/N_2} = 3.3−4.4 of Basolite A100.[43] The good agreement between the experimental data and the literature data demonstrates the validation of the homemade apparatus for breakthrough measurements.

The values of selectivity of α_{CH_4/N_2} for Sample **1a**, **1b** and **1c** are respectively 5.6−6.0, 5.9−6.1 and 5.5−5.9, which are nearly constant and in good agreement with the ideal selectivities of S_{CH_4/N_2} = 5.7−6.1, determined by ratio of the Henry's law constants. Sample **2a** exhibits higher selectivity of α_{CH_4/N_2} = 7.2−7.5 while Sample **2b** shows lower values around α_{CH_4/N_2} = 4.8−5.1. According to the earlier study, the high selectivities of separating CH_4 over N_2 for $[Ni_3(HCOO)_6]$ frameworks are ascribed to the tight coupling between uniform ultra-micropore (< 7 Å) and moderate polarizability resulting from their peculiar structures where multiple coordination modes exist in the frameworks. Since there is no significant change in the crystalline framework of $[Ni_3(HCOO)_6]$ samples synthesized from different routes, the notable changes in the ultra-micropore volume as well as the pore size dominantly give rise to the different separation performances of CH_4/N_2 mixtures. As we can see, the larger micropore volume the sample has, the higher selectivities for the separation of

CH_4 against N_2 we can obtain. In the meanwhile, large pore size (> 7 Å) also accounts for the lower selectivity.

Additionally, the selectivities of zeolites including 5A, 13X and SAPO-34 we calculated are in good agreement with literature data where 5A and 13X zeolites exhibit selectivities around α_{CH_4/N_2} = 2.0 and α_{CH_4/N_2} = 2.3, respectively,[61,62] SAPO-34 shows values lower than α_{CH_4/N_2} = 3.0.[20] Comparison with other MOFs on the separation of CH_4/N_2 mixtures is not yet possible because of the lack of experimental mixture separation data. Nevertheless, based on the ideal selectivities S_{CH_4/N_2} predicted by the pure gas isotherms, Saha *et al.* showed that MOF-5 and MOF-177 exhibit ideal selectivities of S_{CH_4/N_2} = 1.1 and S_{CH_4/N_2} = 4.0, respectively.[39] Möllmer *et al.* calculated the selectivities of S_{CH_4/N_2} = 4.0-4.4 and S_{CH_4/N_2} = 3.4-4.4 for $^3{}_\infty$[Cu(Me-4py-trz-ia)] and Basolite® A100 at 298 K, respectively.[43] MIL-53(Al) exhibits the ideal selectivities of S_{CH_4/N_2} = 2.7 at 303 K, determined by Rallapalli *et al*.[63] Clearly, all the selectivities for MOFs studied for the separation of CH_4/N_2 are much lower than those of Sample **2a**. Fig. 8 shows the typical breakthrough curves of the CH_4-N_2 equimolar mixture at 298 K on $[Ni_3(HCOO)_6]$ samples at 2.0 bar and on Sample **2a** at 4.0 bar. For all the samples, N_2 breaks first, indicating that N_2 is more weakly adsorbed than CH_4. A marked roll-up effect is observed in the breakthrough curves of N_2 just before CH_4 breaks. The momentary higher concentration of N_2 in the eluting gas than in the feed gas is due to partial desorption of N_2 when CH_4 competitively adsorbs in the column.[44] The equilibrium selectivities calculated from the breakthrough curves in Fig. 8 are determined to be 6.0 for Sample **1a**, 5.9 for Sample **1b**, 5.8 for Sample **1c**, 7.2 for Sample **2a** and 4.8 for Sample **2b** at 298 K and 2.0 bar. Sample **2a** presents the selectivity of α_{CH_4/N_2} = 7.5 at 298 K and 4.0 bar according to Fig. 8F. All the CH_4/N_2 selectivities determined from the breakthrough curves on other samples are showed in the Fig. 7.

For practical use, a desired adsorbent should not only possess high selectivity and high adsorption capacity, but also display a stable cyclic adsorption performance during long-term

cyclical operation. Here, we have carried out cyclical adsorptive separation experiments at 298 K. All the synthesized $[Ni_3(HCOO)_6]$ frameworks can be fully regenerated by purging with helium and show fairly consistent performance in the separation of CH_4 and N_2. Clearly seen from the breakthrough curves measured at 298 K and 4.0 bar for Sample **2a** (Fig. 9), the separation performances are constant for several repeat cycles after regeneration. Meanwhile, for Sample 1a, after 20 cycles of separation experiments at 298 K, 6.0 bar, the separation selectivities are nearly constant as showed in Fig. S19 (see ESI).

Activated carbons have also been extensively studied on the separation of CH_4/N_2 mixtures. The average selectivities over activated carbon are *ca*. 1.9−4.0,[8-11] much lower than $[Ni_3(HCOO)_6]$ frameworks. The large uniform ultra-micropore (< 7 Å) volume coupled with moderate polarizability resulting from the multiple coordination modes for $[Ni_3(HCOO)_6]$ frameworks provides an enhanced adsorption potential towards CH_4.[44] On the other hand, the weak polar surface and chaotic pore structure limit the separation selectivity of CH_4/N_2 mixture for activated carbons[1]. As compared with 5A zeolite and the BPL carbon, one of the most intensively studied activated carbons, $[Ni_3(HCOO)_6]$ frameworks show the enhanced higher selectivities up to triple values of 5A zeolite and BPL carbon (Table 4), making them to be good candidates for preferential adsorption of CH_4 against N_2.

4. Conclusions

In this work, we have successfully optimized the synthesis of the ultra-microporous $[Ni_3(HCOO)_6]$ frameworks by changing the precursors. Pore structures including ultra-micropore volumes, surface areas and pore size distributions are tuned to improve the CH_4/N_2 separation performances, which are evaluated by pure gas adsorption measurements and binary gas breakthrough experiments. Based on the characterizations of the samples, the larger ultra-micropore volume corresponds to the

higher selectivities. Sample **2a** synthesized by non-corrosive methyl formate and nickel nitrate shows the largest ultra-micropore volume and exhibits an enhanced high selectivity of α_{CH_4/N_2} = 7.2−7.5 for the separation of CH_4/N_2 in the pressure range of 2.0−10 bar. The sample can also be easily regenerated and presents constant separation performances after cyclical adsorptive separation experiments. The results of XRD, FT-IR, SEM, TGA/DSC and Ar adsorption indicate that Sample **2a** displays good crystallization, uniform crystal size (~ 140 nm) and permanent porosity. The good separation performances presented by Sample **2a** make it a promising candidate as a sustainable and effective adsorbent for upgrading low-quality natural gas.

Acknowledgements

This work was supported by grants from the National High Technology Research and Development Program of China (863 Program, 2009AA050902) and the Innovation Fund of the Chinese Academy of Sciences (K20110812). We are also grateful to Prof. Haiyang Liand Dr. Keyong Hou for their advanced mass spectrometer technology.

References

1. R. T. Yang, *Adsorbent: Fundametals and Applications*, John Wiley & Sons, Hoboken, 2003.
2. A. J. Kidnay and W. R. Parrish, *Fundamentals of Natural Gas Processing*, 2nd edn., CRC Press, Boca Raton, 2006.
3. A. Jayaraman, A. J. Hernandez-Maldonado, R. T. Yang, D. Chinn, C. L. Munson and D. H. Mohr, *Chem. Eng. Sci.*, 2004, **59**, 2407-2417.
4. M. Tagliabue, D. Farrusseng, S. Valencia, S. Aguado, U. Ravon, C. Rizzo, A. Corma and C. Mirodatos, *Chem. Eng. J.*, 2009, **155**, 553-566.
5. *US Pat.*, 20120036890, 2012.
6. K. A. Lokhandwala, I. Pinnau, Z. He, K. D. Amo, A. R. DaCosta, J. G. Wijmans and R. W. Baker, *J. Membr. Sci.*, 2010, **346**, 270-279.
7. K. Lee, W. C. Isley, A. L. Dzubak, P. Verma, S. J. Stoneburner, L.-C. Lin, J. D. Howe, E. D. Bloch, D. A. Reed, M. R. Hudson, C. M. Brown, J. R. Long, J. B. Neaton, B. Smit, C. J. Cramer, D. G. Truhlar and L. Gagliardi, *J. Am. Chem. Soc.*, 2014, **136**, 698-704.
8. M. S. A. Baksh, R. T. Yang and D. D. L. Chung, *Carbon*, 1989, **27**, 931-934.
9. B. Yuan, X. Wu, Y. Chen, J. Huang, H. Luo and S. Deng, *J. Colloid Interface Sci.*, 2013, **394**, 445-450.
10. H. Yi, F. Li, P. Ning, X. Tang, J. Peng, Y. Li and H. Deng, *Chem. Eng. J.*, 2013, **215-216**, 635-642.
11. B. Yuan, X. Wu, Y. Chen, J. Huang, H. Luo and S. Deng, *Environ. Sci. Technol.*, 2013, **47**, 5474-5480.
12. J. A. Delgado, M. A. Uguina, J. L. Sotelo and B. Ruíz, *Sep. Purif. Technol.*, 2006, **50**, 192-203.
13. J. A. Delgado, M. A. Uguina, J. L. Sotelo, V. I. Agueda and P. Gomez, *Sep. Purif. Technol.*, 2011, **77**, 7-17.

14. P. B. Lederman and B. Williams, *AIChE J.*, 1964, **10**, 30-34.
15. D. M. Ruthven, *AIChE J.*, 1976, **22**, 753-759.
16. P. Li and F. H. Tezel, *Microporous Mesoporous Mater.*, 2007, **98**, 94-101.
17. J. Yang, J. Li, W. Wang, L. Li and J. Li, *Ind. Eng. Chem. Res.*, 2013, **52**, 17856-17864.
18. N. K. Jensen, T. E. Rufford, G. Watson, D. K. Zhang, K. I. Chan and E. F. May, *J. Chem. Eng. Data*, 2012, **57**, 106-113.
19. S. M. Kuznicki, V. A. Bell, S. Nair, H. W. Hillhouse, R. M. Jacubinas, C. M. Braunbarth, B. H. Toby and M. Tsapatsis, *Nature*, 2001, **412**, 720-724.
20. M. E. Rivera-Ramos and A. J. Herna´ndez-Maldonado, *Ind. Eng. Chem. Res.*, 2007, **46**, 4991-5002.
21. K. Sumida, D. L. Rogow, J. A. Mason, T. M. McDonald, E. D. Bloch, Z. R. Herm, T.-H. Bae and J. R. Long, *Chem. Rev.*, 2012, **112**, 724-781.
22. Y.-S. Bae and R. Q. Snurr, *Angew. Chem. Int. Ed.*, 2011, **50**, 11586-11596.
23. D. M. D'Alessandro, B. Smit and J. R. Long, *Angew. Chem. Int. Ed.*, 2010, **49**, 6058-6082.
24. S. Chaemchuen, N. A. Kabir, K. Zhou and F. Verpoort, *Chem. Soc. Rev.*, 2013, **42**, 9304-9332.
25. J. Liu, P. K. Thallapally, B. P. McGrail, D. R. Brown and J. Liu, *Chem. Soc. Rev.*, 2012, **41**, 2308.
26. T. E. Rufford, S. Smart, G. C. Y. Watson, B. F. Graham, J. Boxall, J. C. Diniz da Costa and E. F. May, *J. Pet. Sci. Eng.*, 2012, **94-95**, 123-154.
27. S. Ma and H.-C. Zhou, *Chem. Commun.*, 2010, **46**, 44.
28. A. U. Czaja, N. Trukhan and U. Müller, *Chem. Soc. Rev.*, 2009, **38**, 1284.
29. L. J. Murray, M. Dincă and J. R. Long, *Chem. Soc. Rev.*, 2009, **38**, 1294.
30. M. P. Suh, H. J. Park, T. K. Prasad and D.-W. Lim, *Chem. Rev.*, 2012, **112**, 782-835.
31. J.-R. Li, R. J. Kuppler and H.-C. Zhou, *Chem. Soc. Rev.*, 2009, **38**, 1477.
32. J.-R. Li, Y. Ma, M. C. McCarthy, J. Sculley, J. Yu, H.-K. Jeong, P. B. Balbuena and H.-C. Zhou, *Coord. Chem. Rev.*, 2011, **255**, 1791-1823.
33. J.-R. Li, J. Sculley and H.-C. Zhou, *Chem. Rev.*, 2012, **112**, 869-932.
34. S. Kitagawa, R. Kitaura and S.-i. Noro, *Angew. Chem. Int. Ed.*, 2004, **43**, 2334-2375.
35. F. A. Almeida Paz, J. Klinowski, S. M. F. Vilela, J. P. C. Tomé, J. A. S. Cavaleiro and J. Rocha, *Chem. Soc. Rev.*, 2012, **41**, 1088.
36. Z. Wang and S. M. Cohen, *Chem. Soc. Rev.*, 2009, **38**, 1315.
37. D. J. Tranchemontagne, J. L. Mendoza-Cortés, M. O'Keeffe and O. M. Yaghi, *Chem. Soc. Rev.*, 2009, **38**, 1257.
38. J. Yang, Q. Yu, Q. Zhao, J. Liang, J. Dong and J. Li, *Microporous Mesoporous Mater.*, 2012, **161**, 154-159.
39. D. Saha, Z. Bao, F. Jia and S. Deng, *Environ. Sci. Technol.*, 2010, **44**, 1820-1826.
40. B. Liu and B. Smit, *Langmuir*, 2009, **25**, 5918-5926.
41. X. Peng, X. Cheng and D. Cao, *J. Mater. Chem.*, 2011, **21**, 11259-11270.
42. B. Liu and B. Smit, *J. Phys. Chem. C*, 2010, **114**, 8515-8522.
43. J. Möllmer, M. Lange, A. Möller, C. Patzschke, K. Stein, D. Lässig, J. Lincke, R. Gläser, H. Krautscheid and R. Staudt, *J. Mater. Chem.*, 2012, **22**, 10274.
44. X. Ren, T. Sun, J. Hu and S. Wang, *Microporous Mesoporous Mater.*, 2014, **186**, 137-145.
45. B. Chen, S. Xiang and G. Qian, *Acc. Chem. Res.*, 2010, **43**, 1115-1124.
46. L. Pan, B. Parker, X. Huang, D. H. Olson, J. Lee and J. Li, *J. Am. Chem. Soc.*, 2006, **128**, 4180-4181.
47. D. Lässig, J. Lincke, J. Moellmer, C. Reichenbach, A. Moeller, R. Gläser, G. Kalies, K. A. Cychosz, M. Thommes, R. Staudt and H. Krautscheid, *Angew. Chem. Int. Ed.*, 2011, **50**, 10344-10348.
48. N. Stock and S. Biswas, *Chem. Rev.*, 2012, **112**, 933-969.
49. P. Maniam and N. Stock, *Inorg. Chem.*, 2011, **50**, 5085-5097.
50. K. Li, D. H. Olsan, J. Y. Lee, W. Bi, K. Wu, T. Yuen, Q. Xu and J. Li, *Adv. Funct. Mater.*, 2008, **18**, 2205-2214.
51. J. Toth, *Adv. Colloid Interface Sci.*, 1995, **55**, 1-239.

52. D. Peralta, G. Chaplais, A. Simon-Masseron, K. Barthelet, C. Chizallet, A.-A. Quoineaud and G. D. Pirngruber, *J. Am. Chem. Soc.*, 2012, **134**, 8115-8126.
53. Z. Wang, B. Zhang, Y. Zhang, M. Kurmoo, T. Liu, S. Gao and H. Kobayashi, *Polyhedron*, 2007, **26**, 2207-2215.
54. M. Viertelhaus, P. Adler, R. Cle´rac, C. E. Anson and A. K. Powell, *Eur. J. Inorg. Chem.*, 2005, **2005**, 692-703.
55. Z. M. Wang, Y. J. Zhang, T. Liu, M. Kurmoo and S. Gao, *Adv. Funct. Mater.*, 2007, **17**, 1523-1536.
56. B. Warren, *X-ray Diffraction*, Addison-Wesley, London, 1989.
57. K. S. Walton and R. Q. Snurr, *J. Am. Chem. Soc.*, 2007, **129**, 8552-8556.
58. S. J. Gregg and K. S. W. Sing, *Adsorption, surface area and porosity*, 2nd edn., Academic Press, New York, 1982.
59. Y. Pan, Y. Liu, G. Zeng, L. Zhao and Z. Lai, *Chem. Commun.*, 2011, **47**, 2071.
60. D. D. Do, *Adsorption Analysis: Equilibria and Kinetics*, Imperial College Press, London, 1998.
61. W. Sievers and A. Mersmann, *Chem. Eng. Technol.*, 1994, **17**, 325-337.
62. S. Cavenati, C. A. Grande and A. r. E. Rodrigues, *J. Chem. Eng. Data*, 2004, **49**, 1095-1101.
63. P. Rallapalli, K. P. Prasanth, D. Patil, R. S. Somani, R. V. Jasra and H. C. Bajaj, *J. Porous Mater.*, 2010, **18**, 205-210.

Figure captions

Fig. 1 Comparison of the experimental powder X-ray diffraction patterns of synthesized $[Ni_3(HCOO)_6]$ samples along with the simulated pattern from Reference [55].

Fig. 2 FT-IR spectroscopy of $[Ni_3(HCOO)_6]$ samples.

Fig. 3 SEM images of $[Ni_3(HCOO)_6]$ samples: (A) and (B) **1a**, (C) and (D) **1b**, (E) and (F) **2a**, (G) **1c** and (H) **2b**.

Fig. 4 TGA curves of $[Ni_3(HCOO)_6]$ samples in argon atmosphere.

Fig. 5 Argon adsorption isotherms of $[Ni_3(HCOO)_6]$ samples: **1a** (red squares); **1b** (blue circles); **1c** (magenta up triangles); **2a** (olive down triangles) and **2b** (navy left triangles) measured at 87.3 K, respectively.

Fig. 6 Pure gas adsorption experiments: adsorption isotherms for CH_4 at 288 K (black squares), 298 K (red cycles) and 308 K (blue up triangles) and N_2 at 288 K (green down triangles), 298 K (magenta diamonds) and 308 K (wine stars) on (A) Sample **1a**; (B) Sample **1b**; (C) Sample **1c**; (D) Sample **2a**; (E) Sample **2b** (Solid lines: Toth model). Toth model nicely fits each CH_4 and N_2 adsorption isotherm on $[Ni_3(HCOO)_6]$ samples.

Fig. 7 CH_4-N_2 selectivity as a function of pressure for $[Ni_3(HCOO)_6]$ samples, zeolites and other MOFs.

Fig. 8 Breakthrough curves of the CH_4-N_2 equimolar mixture on $[Ni_3(HCOO)_6]$ samples at 298 K for (A) Sample **1a**, (B) Sample **1b**, (C) Sample **1c**, (D) Sample **2a**, (E) Sample **2b** at 2.0 bar and (F) Sample **2a** at 4.0 bar.

Fig. 9 Breakthrough curves on Sample **2a** for five repeated cycles at 298 K and 4.0 bar.

Fig. 1 Comparison of the experimental powder X-ray diffraction patterns of synthesized $[Ni_3(HCOO)_6]$ samples along with the simulated pattern from Reference [55].

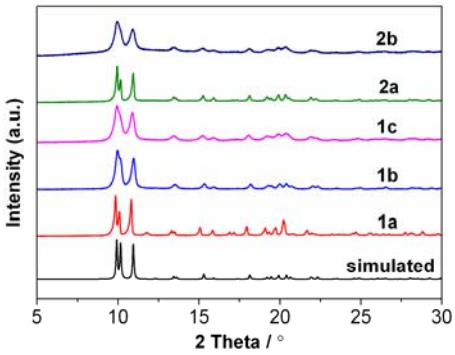

Fig. 2 FT-IR spectroscopy of $[Ni_3(HCOO)_6]$ samples.

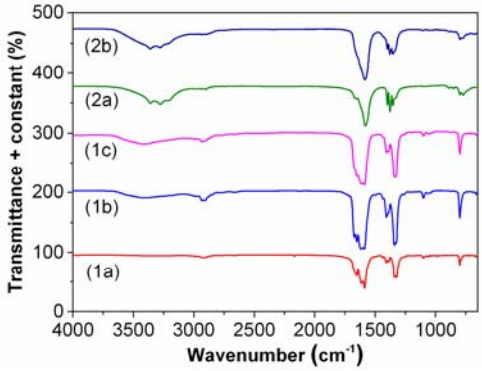

Fig. 3 SEM images of $[Ni_3(HCOO)_6]$ samples: (A) and (B) **1a**, (C) and (D) **1b**, (E) and (F) **2a**, (G) **1c** and (H) **2b**.

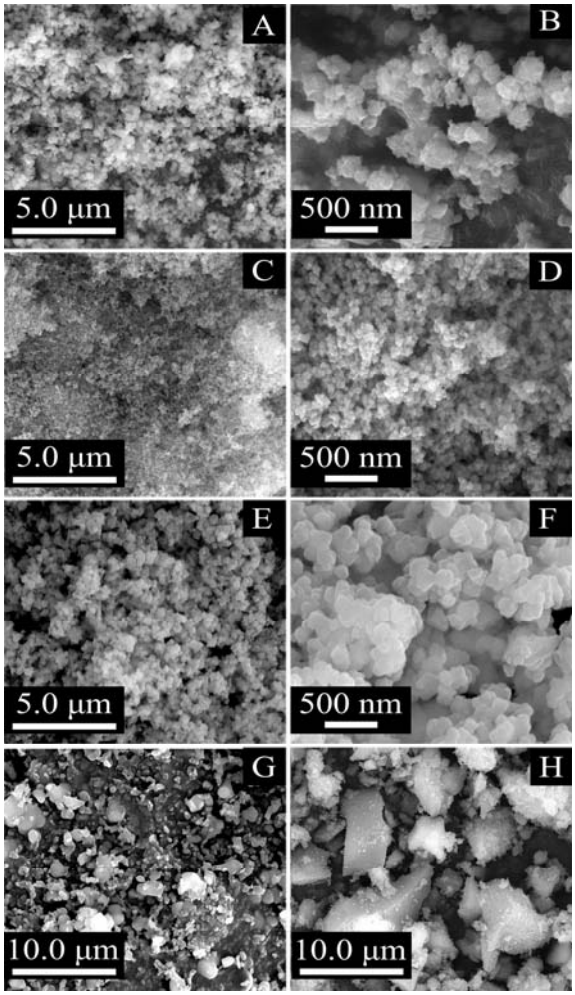

Fig. 4 TGA curves of $[Ni_3(HCOO)_6]$ samples in argon atmosphere.

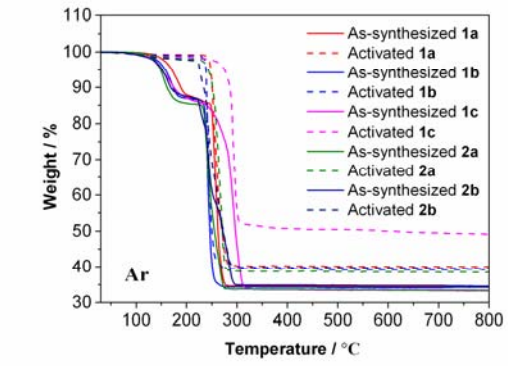

Fig. 5 Argon adsorption isotherms of $[Ni_3(HCOO)_6]$ samples: **1a** (red squares); **1b** (blue circles); **1c** (magenta up triangles); **2a** (olive down triangles) and **2b** (navy left triangles) measured at 87.3 K, respectively.

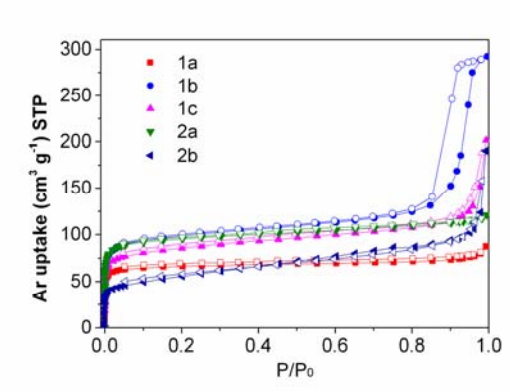

Fig. 6 Pure gas adsorption experiments: adsorption isotherms for CH_4 at 288 K (black squares), 298 K (red cycles) and 308 K (blue up triangles) and N_2 at 288 K (green down triangles), 298 K (magenta diamonds) and 308 K (wine stars) on (A) Sample **1a**; (B) Sample **1b**; (C) Sample **1c**; (D) Sample **2a**; (E) Sample **2b** (Solid lines: Toth model). Toth model nicely fits each CH_4 and N_2 adsorption isotherm on $[Ni_3(HCOO)_6]$ samples.

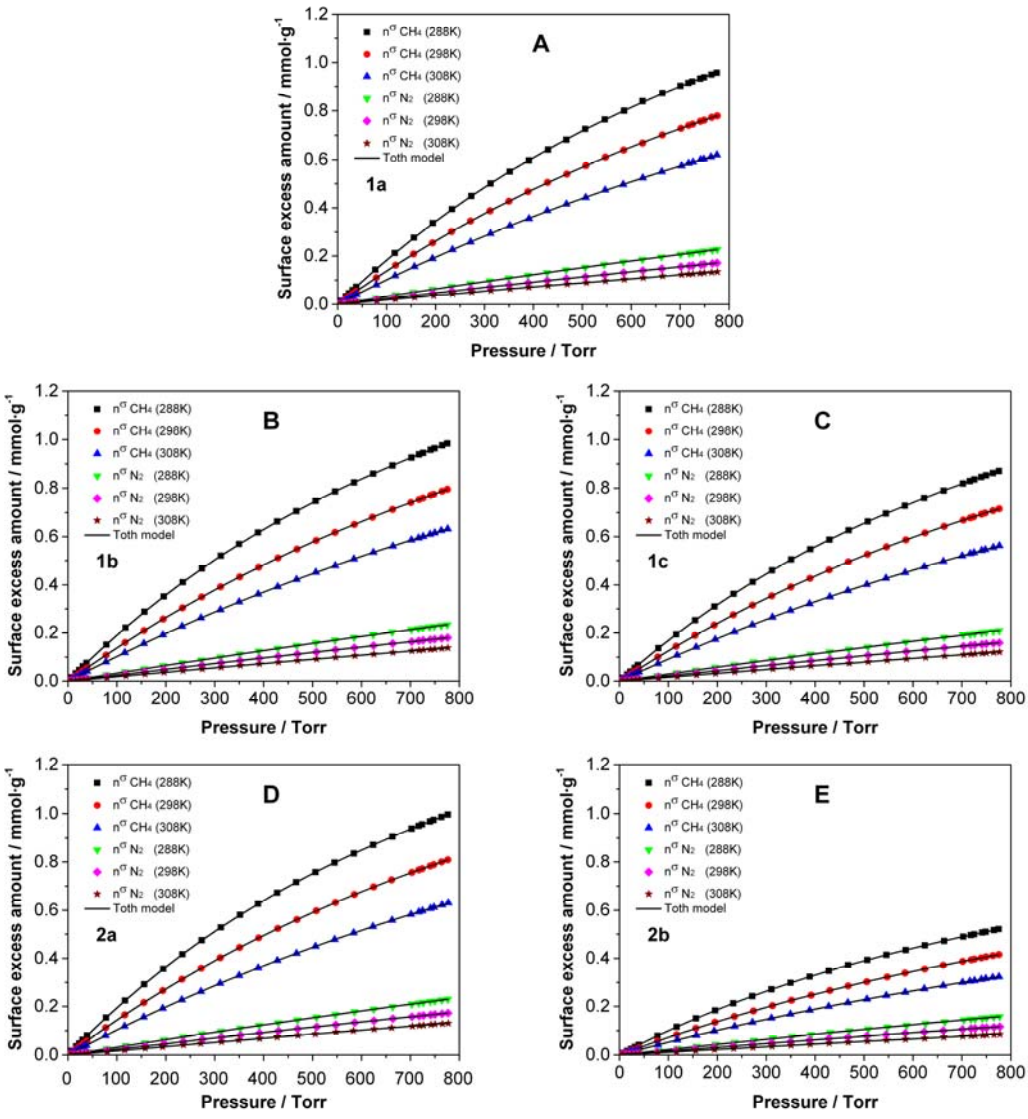

Fig. 7 CH_4-N_2 selectivity as a function of pressure for $[Ni_3(HCOO)_6]$ samples, zeolites and other MOFs.

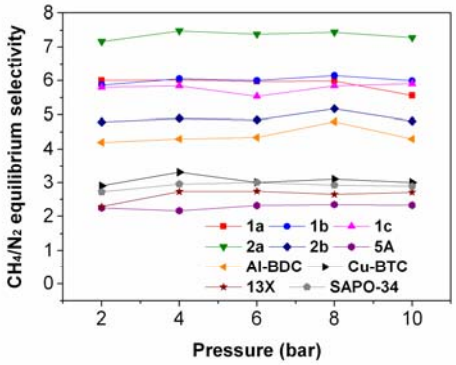

Fig. 8 Breakthrough curves of the CH_4-N_2 equimolar mixture on $[Ni_3(HCOO)_6]$ samples at 298 K for (A) **1a**, (B) **1b**, (C) **1c**, (D) **2a**, (E) **2b** at 2.0 bar and (F) **2a** at 4.0 bar.

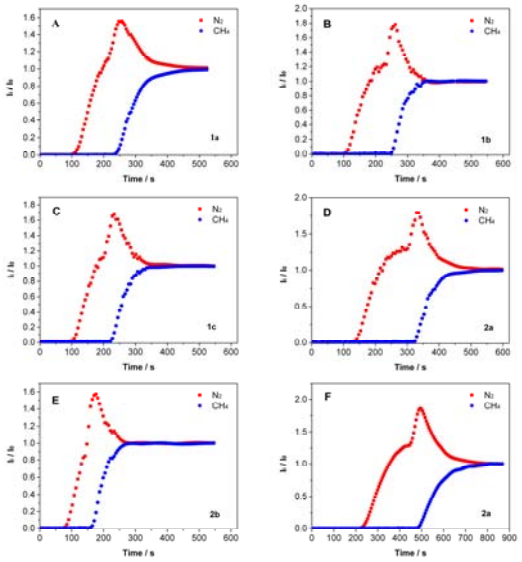

Fig. 9 Breakthrough curves on Sample **2a** for five repeated cycles at 298 K and 4.0 bar.

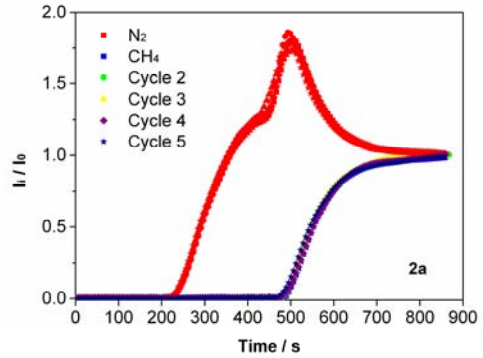

Table caption

Table 1 Yield and crystallinity data of $[Ni_3(HCOO)_6]$ samples synthesized by different routes. ND, no data.

Table 2 Porosity data of $[Ni_3(HCOO)_6]$ samples synthesized by different routes based on Ar adsorption isotherms. S_{BET} and S_{Lang} are the BET and Langmuir surface areas, respectively. V_t and V_{mic} are the total pore volume and micropore volume, respectively.

Table 3 Ideal selectivities at zero coverage calculated from Henry's law constants determined by pure gas Toth isotherm parameters.

Table 4 Comparison of CH_4/N_2 separation selectivity of $[Ni_3(HCOO)_6]$ samples, BPL carbon and 5A zeolite at 298 K and 2.0 bar.

Table 1 Yield and crystallinity data of $[Ni_3(HCOO)_6]$ samples synthesized by different routes. ND, no data.

Sample Number	Nickel precursor	HCOO- precursor	Product yield (%)	Crystallinity (%)
1a	Nitrate	FA	100	99.11
1b	Acetate	FA	97.8	94.06
1c	Chloride	FA	95.1	92.06
2a	Nitrate	MF	100	99.91
2b	Acetate	MF	100	82.57
2c	Chloride	MF	1.69	ND

Table 2 Porosity data of $[Ni_3(HCOO)_6]$ samples synthesized by different routes based on Ar adsorption isotherms. S_{BET} and S_{Lang} are the BET and Langmuir surface areas, respectively. V_t and V_{mic} are the total pore volume and micropore volume, respectively.

Sample Number	S_{BET} (m^2/g)	P/P_0 range for S_{BET} [a]	S_{Lang} (m^2/g)	P/P_0 range for S_{Lang} [b]	V_t [c] (cm^3/g)	V_{mic} [d] (cm^3/g)	NLDFT PSD (Å)
1a	232	0.005-0.0427	262	0.0533-0.3032	0.097	0.078	6.12
1b	331	0.007-0.0529	410	0.0529-0.3525	0.350	0.085	6.42 213
1c	284	0.007-0.0530	362	0.0530-0.3522	0.166	0.074	6.42
2a	327	0.007-0.0534	386	0.0534-0.3528	0.146	0.097	6.42
2b	173	0.0100-0.1517	292	0.1517-0.3520	0.130	0.022	8.30 18.71

[a]The linearity of fitting for BET model is 0.9999. [b]The linearity of fitting for Langmuir model is 0.999. [c]V_t (total pore volume) calculated by Gurvich-rule at P/P_0=0.95. [d]V_{mic} (micropore volume) calculated by *t*-Plot method.

Table 3 Ideal selectivities at zero coverage calculated from Henry's law constants determined by pure gas Toth isotherm parameters.

Sample Number	Ideal Selectivity S_{CH_4/N_2}		
	288 K	298 K	308 K
1a	6.0	6.1	5.7
1b	6.1	5.8	5.7
1c	6.1	6.0	5.8
2a	6.6	6.5	6.2
2b	4.8	4.7	4.8

Table 4 Comparison of CH_4/N_2 separation selectivity of $[Ni_3(HCOO)_6]$ samples, BPL carbon and 5A zeolite at 298 K and 2.0 bar.

Material	Gas pairs	$[Ni_3(HCOO)_6]$ selectivity	BPL carbon selectivity [7]	5A zeolite selectivity	Ratio $[Ni_3(HCOO)_6]$ /BPL carbon	Ratio $[Ni_3(HCOO)_6]$ /5A zeolite
1a	CH_4/N_2	6.0	2.4	2.2	2.5	2.7
1b	CH_4/N_2	5.9	2.4	2.2	2.5	2.7
1c	CH_4/N_2	5.8	2.4	2.2	2.4	2.6
2a	CH_4/N_2	7.2	2.4	2.2	3.0	3.3
2b	CH_4/N_2	4.8	2.4	2.2	2.0	2.2

Graphical Abstract

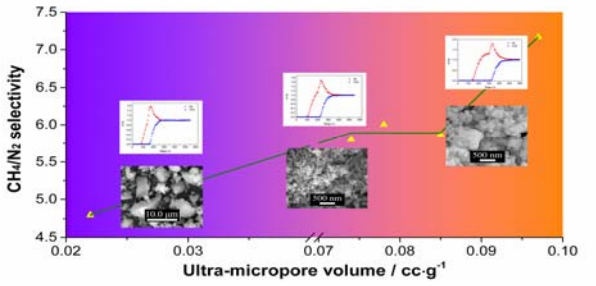

The adsorptive separation selectivities of CH_4/N_2 were successfully improved from 4.0−4.8 to 7.0−7.5 via synthesis optimization of the ultra-microporous $[Ni_3(HCOO)_6]$ frameworks.